PHYSICAL REVIEW C **79**, 064308 (2009)

Depletion of the nuclear Fermi sea

Arnau Rios*
National Superconducting Cyclotron Laboratory and Department of Physics and Astronomy, Michigan State University, East Lansing, Michigan 48824-1321, USA

Artur Polls
Departament d'Estructura i Constituents de la Matèria and Institut de Ciències del Cosmos, Universitat de Barcelona, Avda. Diagonal 647, E-08028 Barcelona, Spain

W. H. Dickhoff
Department of Physics, Washington University, St. Louis, Missouri 63130, USA
(Received 14 April 2009; published 10 June 2009)

The short-range and tensor components of the bare nucleon-nucleon interaction induce a sizable depletion of low momenta in the ground state of a nuclear many-body system. The self-consistent Green's function method within the ladder approximation provides an *ab initio* description of correlated nuclear systems that accounts properly for these effects. The momentum distribution predicted by this approach is analyzed in detail, with emphasis on the depletion of the lowest momentum state. The temperature, density, and nucleon asymmetry (isospin) dependence of the depletion of the Fermi sea is clarified. A connection is established between the momentum distribution and the time-ordered components of the self-energy, which allows for an improved interpretation of the results. The dependence on the underlying nucleon-nucleon interaction provides quantitative estimates of the importance of short-range and tensor correlations in nuclear systems.

DOI: 10.1103/PhysRevC.79.064308 PACS number(s): 21.60.De, 21.65.Cd

I. INTRODUCTION

Recent experiments at Jefferson Laboratory have clarified several aspects of the role of short-range and tensor correlations in determining the properties of nucleons in the nuclear medium. In an $(e, e'p)$ experiment on ^{12}C, an unambiguous signature of the presence of high-momentum nucleons was identified [1]. In the domain of missing energy and momentum probed by the experiment, the amount of single-particle (sp) strength identified corresponded reasonably to scaled theoretical predictions of the self-consistent Green's function (SCGF) calculation for ^{16}O [2] and correlated basis functions (CBF) calculations for nuclear matter in the local density approximation [3]. The underlying mechanism for the presence of these high-momentum components is associated with the strong repulsion that nucleons experience when they are in close proximity, generating a suppression of the relative wave function in coordinate space. In turn, this repulsion is required by the experimental nucleon-nucleon (NN) phase shifts. An additional mechanism that provides high-momentum components is the action of the NN tensor force, mediated to a large extent by the exchange of the pion.

In even more demanding exclusive two-nucleon knock-out experiments on ^{16}O to the ground state of ^{14}C [4,5], direct evidence for the presence of short-range proton-proton (pp) correlations was identified, in reasonable agreement with theoretical calculations [6,7]. Definitive evidence for the importance of the nuclear tensor force in generating high-momentum components was presented in Ref. [8], where the ratio of knocked-out proton-neutron (pn) to pp pairs from ^{12}C was found to be around 20. Theoretical relative momentum distributions exhibit a similar enhancement of pn over pp correlations due to the tensor force in the domain of momenta probed in this Jefferson Lab experiment [9]. Possible implications for the physics of neutron stars were discussed in Ref. [10].

Particle number conservation requires the high-momentum components to be accompanied by a corresponding depletion of the nuclear Fermi sea. A characteristic feature of this depletion in nuclear matter is its essentially momentum-independent character, except in the immediate vicinity of the Fermi surface [11]. A survey of calculations [12–15] of the momentum distribution of nuclear matter at normal density in Ref. [11] demonstrated that, for all realistic NN interactions then available, different many-body techniques consistently predicted a depletion of the nuclear Fermi sea of a little over 15%. About one-third of this depletion results from tensor correlations. In addition, the influence of three-body forces on the depletion appears to be rather insignificant [12]. An $(e, e'p)$ experiment on ^{208}Pb at National Institute for Nuclear Physics and High Energy Physics (NIKHEF) in a large domain of missing energy and a momentum range corresponding to the mean-field Fermi sea confirmed that a global depletion between 15 and 20% of proton orbits below the Fermi energy explains all the measured coincidence cross sections [16,17]. To put these results in perspective it is useful to note that the depletion of liquid ^{3}He for very small momenta is considerably larger and reaches about 50% [18], while the depletion of the electron Fermi sea in closed-shell atoms is essentially zero [19].

Although there is uncertainty about the precise nature of the short-range part of the NN interaction, there is now evidence from recent lattice QCD calculations that the features of a

*rios@nscl.msu.edu

strong repulsive short-range core emerge from first principles, particularly when the pion mass is reduced toward more realistic values [20]. The presence of short-range correlations is thus corroborated by QCD simulations and strongly suggests that fully microscopic nuclear many-body calculations should continue to address their consequences in detail. Recently developed realistic NN interactions, like CDBonn [21,22] or the chiral interactions [23] have in general softer cores than older potentials [24,25]. Even modern local potentials, such as Argonne v18 (Av18) [26], have a soft core compared to more traditional interactions. By assessing the different results for the Av18 and CDBonn interactions in the present article, we plan to develop a measure of the remaining uncertainty of the role of short-range and tensor correlations in nuclei.

A particularly well-suited technique for this goal is the SCGF method [27]. Within this approach, a fully self-consistent treatment of ladder diagrams for the interaction between particles that propagate with respect to a correlated (by short-range and tensor effects) ground state are accounted for. Recently, calculations including full off-shell effects have become available at finite temperature [28–31], providing thermodynamically consistent results that preserve sum rules, like, e.g., conservation of the number of particles [32,33]. Earlier applications of this approach at $T = 0$ involved a discretized version of the spectral distribution and have challenged the conventional interpretation of the nuclear-matter saturation problem [34]. Finite-temperature effects are expected to smooth out the momentum distribution near the Fermi momentum, not unlike the influence of pairing correlations [25]. Thermal effects hardly affect the small and very high-momentum content of the ground state, however. This expectation is confirmed in general by the present work, although it requires some qualification in the case of low density or high temperatures, as we shall discuss in this work.

The study of the asymmetry dependence of short-range and tensor correlations is motivated to a large extent by the (future) study of rare isotopes with large neutron excess. Experimental studies employing heavy-ion knock-out reactions already suggest that the removal probability for the minority species is strongly reduced compared to shell-model calculations, whereas the majority species exhibits properties that are essentially mean-field like [35]. Similar tendencies, but smaller in magnitude, have been obtained for the spectroscopic factors of protons from a combined dispersive optical model analysis of a sequence of Ca isotopes [36,37]. Fitting a huge collection of elastic proton scattering data while including results obtained from $(e, e'p)$ reactions for quantities below the Fermi energy, the emerging complex optical potentials for protons exhibit a striking increase in surface absorption with increasing nucleon asymmetry. This translates into a qualitatively similar tendency in spectroscopic factors as obtained from the zero-momentum occupation of protons calculated in the bulk for isospin-polarized nuclear matter [24]. A major purpose of the present work is to clarify the role of various variables, such as the temperature, the density or the choice of the NN interaction, in the determination of the momentum distribution for isospin-polarized systems. In this fashion, we can assess the importance of the short-range and tensor contributions to the bulk properties of asymmetric nuclei.

Recent applications of the SCGF method to isospin imbalanced matter have generated predictions for the depletion of the proton and the neutron Fermi seas at fixed total density as a function of nucleon asymmetry [24]. Some intriguing results were reported in this work that require a deeper understanding. First, an increasing difference between the zero-momentum occupation of the neutron and proton Fermi sea was reported at a temperature corresponding to 10 MeV. Naively, this difference is expected to be associated with the decreasing (increasing) importance of the nuclear tensor force for neutrons (protons) with increasing asymmetry, because neutrons alone do not experience the strong $^3S_1$-$^3D_1$ tensor coupling, whereas protons will. There are, however, other physical effects that can influence this difference and it is therefore useful to investigate whether the calculated predictions depend on the choice of the realistic interaction or on the temperature. Another feature that requires a better understanding is the opposite density dependence of the depletion for symmetric and pure neutron matter (PNM) reported in Ref. [24]. For symmetric nuclear matter (SNM), a *decrease* in the depletion of the zero-momentum state with increasing density is obtained, while the opposite result pertains for PNM in the case of the CDBonn interaction [21]. The result for SNM differs from earlier calculations, like those reported in Ref. [15] for a separable version [38] of the Paris interaction [39], which predicted very little density dependence of this quantity. We propose to clarify this issue in the present work by analyzing more carefully the ingredients that determine the density dependence of the depletion, paying particular attention to the importance of thermal effects and to the choice of the interaction. To provide a better insight into these dependences, we have relied and further clarified an approximate relation between the momentum distribution, above and below the Fermi surface, and the energy derivatives of the time-ordered components of the self-energy. These components differ from the retarded quantities that have been used in finite-temperature calculations.

In Sec. II, we present the relevant ingredients of the formalism of the finite-temperature implementation of the SCGF method. Results for SNM and PNM are presented in Sec. III, where the role of the temperature, the density, and the choice of realistic interaction (softer vs. harder core) are clarified. A deeper insight into the density and isospin-polarization dependence of the results is obtained by employing the relation between the momentum distribution and energy derivatives of the different time-ordered components of the nucleon self-energy. This topic is discussed in Sec. IV. Results for isospin-polarized matter are analyzed in Sec. V and further interpreted with the help of the relations discussed in Sec. IV. Finally, conclusions are drawn in Sec. VI.

II. SELF-CONSISTENT GREEN'S FUNCTIONS METHOD AT FINITE TEMPERATURE

A. Single-particle propagators

The results that are presented in the following have been obtained with the SCGF method at finite temperature. In quantum statistical mechanics, the expectation value of any

operator $\hat{X}$ is given by a grand-canonical average,

$$\langle \hat{X} \rangle = \frac{\sum_n e^{-\beta(E_n-\mu N_n)} \langle n|\hat{X}|n\rangle}{\sum_n e^{-\beta(E_n-\mu N_n)}}, \tag{1}$$

where $\beta = 1/T$ is the inverse temperature and μ is the chemical potential of the system [32,40,41]. The many-body eigenstates of the system, $|n\rangle$, diagonalize simultaneously the Hamiltonian and the particle number operators,

$$\hat{H}|n\rangle = E_n|n\rangle, \tag{2}$$
$$\hat{N}|n\rangle = N_n|n\rangle, \tag{3}$$

and their Boltzmann sum [the denominator of Eq. (1)] defines the partition function of the system, $\mathcal{Z}$. These eigenstates contain all the micro- and macroscopic information of the system, but an *ab initio* calculation including all of them is intractable. The description of the system can be substantially simplified, without loosing physical information, by considering particular kinds of excitations on top of the thermal bath. At the *sp* level, for instance, all the information of a homogeneous quantum many-body system is encoded in the time-ordered one-body propagator,

$$i\mathcal{G}_{\mathcal{T}}(k;t-t') = \langle \mathcal{T}[\hat{a}_k(t)\hat{a}_k^\dagger(t')]\rangle, \tag{4}$$

given by the thermal average of a product of Heisenberg-picture operators associated with the addition and removal of *sp* excitations with momentum k between times t and t'. The time-ordering is implemented by the Wick operator, $\mathcal{T}$, which arranges the operators in a chronological order and incorporates a $+1$ (-1) factor according to the even (odd) nature of the corresponding permutation [40,41]. The ordering of the time variable determines the analytical structure of $\mathcal{G}_{\mathcal{T}}$ in the Fourier space associated with the time difference, $t-t'$.

The correlation functions,

$$i\mathcal{G}^>(k;t-t') = \langle \hat{a}_k(t)\hat{a}_k^\dagger(t')\rangle \tag{5}$$
$$i\mathcal{G}^<(k;t-t') = -\langle \hat{a}_k^\dagger(t')\hat{a}_k(t)\rangle, \tag{6}$$

are equal to the time-ordered propagator in the corresponding $t > t'$ and $t < t'$ domains. Because of the absence of time-ordering, $\mathcal{G}^>$ and $\mathcal{G}^<$ are analytical and well-defined functions at all energies. The Lehmann representation for $\mathcal{G}^>$,

$$\mathcal{G}^>(k,\omega) = 2\pi \sum_{n,m} \frac{e^{-\beta(E_n-\mu N_n)}}{\mathcal{Z}} |\langle m|\hat{a}_k^\dagger|n\rangle|^2 \delta(\omega - E_m + E_n), \tag{7}$$

provides a physical interpretation for this function, as the probability of adding a particle with momentum k on top of the thermal bath and ending up in any possible final state, m, as long as the energy difference between the states coincides with ω. A similar interpretation exists for $\mathcal{G}^<$ in terms of the removal of a particle from the bath. For a system in thermal equilibrium, the correlation functions are connected by detailed balance,

$$\mathcal{G}^<(k,\omega) = e^{\beta(\omega-\mu)}\mathcal{G}^>(k,\omega), \tag{8}$$

yielding the so-called Kubo-Martin-Schwinger (KMS) relation [32]. The sum of $\mathcal{G}^>$ and $\mathcal{G}^<$ defines the *sp* spectral function of the system, $\mathcal{A}(k,\omega)$, which is individually linked to either of them by the relations,

$$\mathcal{G}^<(k,\omega) = f(\omega)\mathcal{A}(k,\omega), \tag{9}$$
$$\mathcal{G}^>(k,\omega) = [1-f(\omega)]\,\mathcal{A}(k,\omega), \tag{10}$$

with $f(\omega) = [1+e^{\beta(\omega-\mu)}]^{-1}$ the Fermi-Dirac distribution.

The retarded propagator

$$i\mathcal{G}_{\mathcal{R}}(k;t-t') = \Theta(t-t')\langle \hat{a}_k(t)\hat{a}_k^\dagger(t')\rangle, \tag{11}$$

is related to the causal propagation of perturbations in the system, as enforced by the presence of the Heaviside function in relative time. Its spectral decomposition in frequency space is given uniquely in terms of the spectral function

$$\mathcal{G}_{\mathcal{R}}(k,\omega) = \int_{-\infty}^{\infty} \frac{d\omega'}{2\pi} \frac{\mathcal{A}(k,\omega')}{\omega_+ - \omega'}, \tag{12}$$

where the notation $\omega_\pm = \omega \pm i\eta$, with η infinitesimally small, has been introduced. Decomposing Eq. (12) in real and imaginary parts,

$$\mathrm{Im}\mathcal{G}_{\mathcal{R}}(k,\omega) = -\frac{1}{2}\mathcal{A}(k,\omega), \tag{13}$$
$$\mathrm{Re}\mathcal{G}_{\mathcal{R}}(k,\omega) = -\mathcal{P}\int_{-\infty}^{\infty} \frac{d\omega'}{\pi} \frac{\mathrm{Im}\mathcal{G}_{\mathcal{R}}(k,\omega')}{\omega-\omega'}, \tag{14}$$

a direct connection between $\mathrm{Im}\mathcal{G}_{\mathcal{R}}$ and the *sp* spectral function is found. Moreover, a dispersion relation ($\mathcal{P}$ denotes a principal part integration) links the real part of $\mathcal{G}_{\mathcal{R}}$ to the energy dependence of its corresponding imaginary part.

Similarly, the spectral decomposition of the time-ordered propagator can be written as the sum of two terms

$$\mathcal{G}_{\mathcal{T}}(k,\omega) = \mathcal{G}_\uparrow(k,\omega) + \mathcal{G}_\downarrow(k,\omega), \tag{15}$$

each of them depending both on the spectral function and an additional phase space factor. The real and imaginary parts of the up,

$$\mathrm{Im}\mathcal{G}_\uparrow(k,\omega) = \frac{1}{2}f(\omega)\mathcal{A}(k,\omega), \tag{16}$$
$$\mathrm{Re}\mathcal{G}_\uparrow(k,\omega) = \mathcal{P}\int_{-\infty}^{\infty} \frac{d\omega'}{\pi} \frac{\mathrm{Im}\mathcal{G}_\uparrow(k,\omega')}{\omega-\omega'}, \tag{17}$$

and the down components,

$$\mathrm{Im}\mathcal{G}_\downarrow(k,\omega) = -\frac{1}{2}[1-f(\omega)]\mathcal{A}(k,\omega), \tag{18}$$
$$\mathrm{Re}\mathcal{G}_\downarrow(k,\omega) = -\mathcal{P}\int_{-\infty}^{\infty} \frac{d\omega'}{\pi} \frac{\mathrm{Im}\mathcal{G}_\downarrow(k,\omega')}{\omega-\omega'}, \tag{19}$$

are linked by independent dispersion relations. It is then easy to show that the retarded propagator is related to the time-ordered components via the expressions:

$$\mathrm{Im}\mathcal{G}_\uparrow(k,\omega) = -f(\omega)\mathrm{Im}\mathcal{G}_{\mathcal{R}}(k,\omega), \tag{20}$$
$$\mathrm{Im}\mathcal{G}_\downarrow(k,\omega) = [1-f(\omega)]\mathrm{Im}\mathcal{G}_{\mathcal{R}}(k,\omega). \tag{21}$$

In the zero-temperature limit, the phase-space factors in the dispersion integrals guarantee that the integration domains for the up and down components are disconnected. The integration in $\mathcal{G}_\uparrow$ goes up to the Fermi surface, $\omega = \mu$, while the dispersion integral for $\mathcal{G}_\downarrow$ starts at this point. Because the poles of the up (down) component are in the upper (lower) half of the

complex energy plane, one can associate the first (second) term to a "hole" ("particle") propagator. In contrast, the dispersion integral associated with $\mathcal{G}_\mathcal{R}$ receives simultaneous contributions from above and below the Fermi surface. As we shall see in the following, this generates rather different energy dependences for the real parts of these three quantities. Let us also note that the knowledge of the spectral function is enough to compute the real and imaginary parts of all the different *sp* propagators [42].

The definition of the time-ordered propagator, Eq. (4), can be generalized to purely imaginary times with the proper treatment of the imaginary time-ordering [32]. The following KMS relation arises

$$\mathcal{G}_\mathcal{T}(k,\tau) = -e^{\beta\mu}\mathcal{G}_\mathcal{T}(k,\tau - i\beta), \tag{22}$$

which demonstrates that $\mathcal{G}_\mathcal{T}$ is a quasiperiodic function along the imaginary time axis. This suggests the following discrete Fourier representation

$$\mathcal{G}_\mathcal{T}(k,\tau) = \frac{1}{-i\beta}\sum_\nu e^{-iz_\nu\tau}\mathcal{G}(k,z_\nu), \tag{23}$$

where $z_\nu = \frac{(2\nu+1)\pi}{-i\beta} + \mu$ correspond to fermionic Matsubara frequencies [40–42]. An analytical continuation of the coefficients in the Fourier transform, $\mathcal{G}(k,z_\nu)$, to continuous complex values of energy can be uniquely defined [43]. The spectral decomposition of this function

$$\mathcal{G}(k,z) = \int_{-\infty}^{\infty}\frac{d\omega'}{2\pi}\frac{\mathcal{A}(k,\omega')}{z-\omega'}, \tag{24}$$

is again uniquely given by the spectral function. Note that the same function, $\mathcal{G}$, contains information on both the time-ordered propagator (when computed at $z = z_\nu$) and the retarded propagator (at $z = \omega_+$). In general, the sums over Matsubara frequencies can be transformed into energy integrals for the retarded components using complex analysis techniques.

In momentum-frequency space, the Dyson equation for the *sp* propagator,

$$\left[z - \frac{k^2}{2m} - \Sigma(k,z)\right]\mathcal{G}(k,z) = 1, \tag{25}$$

reduces to an algebraic equation in terms of the self-energy, $\Sigma(k,z)$. As a consequence of this equation, the self-energy inherits the analytical properties of the propagator. In particular, it can be decomposed in equivalent retarded, time-ordered or "less/greater than" contributions [42]. Taking the $z \to \omega_+$ limit in this last expression leads to a Dyson equation relating the retarded Green's functions and the retarded self-energy. Because these retarded components form a closed set of equations by themselves, they have been extensively discussed, particularly in the nuclear context at finite temperature [29,44,45]. If one needs to distinguish between particle and hole contributions, however, time-ordered components become essential [44]. The decomposition in terms of up and down self-energies also allows for a more natural connection with zero-temperature SCGF calculations [46,47].

B. Ladder approximation

The retarded self-energy fulfills the dispersion relation

$$\mathrm{Re}\,\Sigma_\mathcal{R}(k,\omega) = \Sigma_{\mathrm{HF}}(k) - \mathcal{P}\int_{-\infty}^{\infty}\frac{d\omega'}{\pi}\frac{\mathrm{Im}\,\Sigma_\mathcal{R}(k,\omega')}{\omega-\omega'}. \tag{26}$$

The first term in this expression corresponds to an energy-independent Hartree-Fock contribution

$$\Sigma_{\mathrm{HF}}(k) = \sum_{k'}\langle \boldsymbol{k}\boldsymbol{k}'|V|\boldsymbol{k}\boldsymbol{k}'\rangle_A n(k'), \tag{27}$$

where we have introduced the NN potential (properly antisymmetrized) and the momentum distribution, $n(k)$. The latter includes correlation effects and can be computed from the *sp* spectral function

$$n(k) = \nu\int_{-\infty}^{\infty}\frac{d\omega}{2\pi}\mathcal{A}(k,\omega)f(\omega), \tag{28}$$

where $\nu = 4(\nu = 2)$ accounts for the degeneracy of nuclear (neutron) matter. The energy-dependent, dispersive contribution to the self-energy describes many-body processes that go beyond the basic mean-field approximation. In the ladder approximation, one includes an infinite series of collisions between a particle and a series of particles and holes in the medium, thus accounting for the two-body scattering problem in the medium [40,41]. The imaginary part of the retarded self-energy in this approximation reads

$$\mathrm{Im}\,\Sigma_\mathcal{R}(k,\omega) = \sum_{k'}\int_{-\infty}^{\infty}\frac{d\omega'}{2\pi}[f(\omega') + b(\omega+\omega')] \times \mathcal{A}(k',\omega')\langle \boldsymbol{k}\boldsymbol{k}'|\mathrm{Im}T(\omega+\omega'_+)|\boldsymbol{k}\boldsymbol{k}'\rangle, \tag{29}$$

and is given in terms of the in-medium interaction, the *sp* spectral function and phase-space factors, including a Bose-Einstein distribution, $b(\Omega) = [e^{-\beta(\Omega-2\mu)} - 1]^{-1}$. The T matrix in the medium fulfills a Lippmann-Schwinger-like equation

$$\begin{aligned}\langle \boldsymbol{k}_1\boldsymbol{k}_2|T(\Omega_+)|\boldsymbol{k}_3\boldsymbol{k}_4\rangle_A &= \langle \boldsymbol{k}_1\boldsymbol{k}_2|V|\boldsymbol{k}_3\boldsymbol{k}_4\rangle_A + \sum_{\boldsymbol{k}_5,\boldsymbol{k}_6}\langle \boldsymbol{k}_1\boldsymbol{k}_2|V|\boldsymbol{k}_5\boldsymbol{k}_6\rangle_A\mathcal{G}^0_{II}(k_5,k_6;\Omega_+) \\ &\times \langle \boldsymbol{k}_5\boldsymbol{k}_6|T(\Omega_+)|\boldsymbol{k}_3\boldsymbol{k}_4\rangle_A,\end{aligned} \tag{30}$$

where the retarded $\mathcal{G}^0_{II}$ is obtained from the product of two spectral functions and a phase-space factor describing the intermediate propagation of particle-particle and hole-hole pairs

$$\mathcal{G}^0_{II}(k,k';\Omega_+) = \int_{-\infty}^{\infty}\frac{d\omega}{2\pi}\frac{d\omega'}{2\pi}\mathcal{A}(k,\omega)\mathcal{A}(k',\omega') \times \frac{1-f(\omega)-f(\omega')}{\Omega_+-\omega-\omega'}, \tag{31}$$

properly accounting for Pauli blocking effects at finite temperature [41]. Once the real and imaginary parts of the self-energy are computed, one can feed back this information into the

spectral function via the Dyson equation

$$\mathcal{A}(k,\omega) = \frac{-2\mathrm{Im}\Sigma_{\mathcal{R}}(k,\omega)}{\left[\omega - \frac{k^2}{2m} - \mathrm{Re}\Sigma_{\mathcal{R}}(k,\omega)\right]^2 + [\mathrm{Im}\Sigma_{\mathcal{R}}(k,\omega)]^2}, \tag{32}$$

which can in turn be used to compute a new $\mathcal{G}^0_{II}$. By iterating this procedure until convergence, the SCGF result within the ladder approximation is obtained. The importance of self-consistency arises from the fact that sum rules are preserved [48,49] and also that thermodynamical consistency is fulfilled [50,51]. In addition, self-consistency represents a democratic treatment of all the particles considered in the problem: the one for which the self-energy is calculated, as well as the ones it interacts with. In all the previous expressions, a grand-canonical ensemble has been assumed, so that there are two external, fixed variables, the temperature and the chemical potential. The latter is not particularly well suited for in-medium studies, so it is customary to supplement the SCGF equations with an equation that fixes the total density of the system

$$\rho = \nu \sum_k n(k,\mu), \tag{33}$$

where we have highlighted the dependence of the momentum distribution on the chemical potential via the Fermi-Dirac factor of Eq. (28).

The numerical solution of the SCGF equations is a demanding task, due to two major difficulties. The first issue is related to the possibility of a pairing solution below a certain critical temperature, T_c, because nucleons tend to form Cooper pairs in certain density regimes [52,53]. Although the SCGF formalism is capable of dealing with the description of the superfluid phase, we will only discuss results for the normal phase, because the effects of pairing are concentrated in a narrow energy region (related to the gap) around the chemical potential [25]. Any conclusion drawn for energies and momenta away from this region should therefore also be valid in the pairing regime and, most interestingly, in the zero-temperature limit. The second numerical difficulty implementing the SCGF method is related to the requirement to solve the coupled nonlinear equations in a wide range of momenta and energies. Because no quasiparticle assumption is made, complete off-shell propagation effects are included. In this case, different regions in the energy and momentum domains have to be sampled simultaneously, particularly the quasiparticle peak and the high-momentum and energy components of the spectral functions. The smoothing of structures associated with finite temperature is helpful in this direction, but the problem is still formidable. It has taken some time before complete, satisfactory numerical results have been obtained for realistic NN interactions. We refer the reader to Refs. [28–31] for further details on how the SCGF is implemented in practice.

Once a self-consistent solution has been obtained, one has access to the spectral functions of a nuclear system at a given density and temperature. In addition to the sp properties, the spectral function also determines to a large extent the macroscopic properties of the system. The total energy, for instance, can be computed from the Galitskii-Migdal-Koltun sum rule [54,55]. An approximation to the entropy beyond the quasiparticle approximation can also be obtained via the Luttinger-Ward formalism [51,56]. All the remaining thermodynamical properties of the system are therefore accessible and include properly the effect of short-range and tensor correlations.

So far, we have discussed uniform nuclear systems with a single species: the nucleon, in the case of SNM, and the neutron, in the case of PNM. For a fixed total density, one can switch from one system to the other by modifying the relative concentration of neutrons and protons. The asymmetry parameter

$$\alpha = \frac{\rho_n - \rho_p}{\rho_n + \rho_p}, \tag{34}$$

is a measure of the isospin imbalance. The SCGF method within the ladder approximation can be generalized to the case of asymmetric nuclear matter and partially isospin-polarized systems can thus be analyzed [24,57,58]. Because the approach accounts for both the short-range and tensor correlations associated with the underlying NN interaction, it can be used to generate quantitative predictions for the importance of different types of correlations in isospin asymmetric systems. In this sense, it is a unique theoretical tool. Other theoretical formalisms either cannot be generalized to isospin asymmetric systems (as is the case of the variational approach [59]) or lack adequate consistency constraints (as in the case of Brueckner-Hartree-Fock theory [60]).

In the following, we shall employ different microscopic NN interactions to quantify the uncertainty related to their short-range and tensor properties. Most of the calculations have been performed with the CDBonn [21] and the Av18 [26] potentials. These phase-shift equivalent forces are representative of two subsets of realistic NN potentials. The first is a boson-exchange potential, with a soft short-range core and a somewhat small tensor component, as indicated by a relatively low D-state probability for the deuteron. The latter is a local potential, with a harder short-range core and a more significant tensor coupling. Although these differences do not affect the two-body scattering observables (which are identical for any phase-shift equivalent interaction), they do influence the in-medium properties due to their different off-shell behaviors [61]. To assess the importance of the different components of the nuclear force, we shall also discuss results obtained from the systematically simplified family of NN interactions obtained by the Argonne group [62]. Each of these forces (from v18 to v4′) has a successively simpler operatorial structure, with their parameters refitted to describe the two-body system at their corresponding level of simplicity. Finally, the Reid93 potential, fitted to the Nijmegen partial wave analysis, has also been used as a benchmark [63]. The momentum distributions obtained with these modern interactions will also be compared to results for older realistic interactions [11] that have somewhat stronger repulsive cores. In all cases, our present results have been obtained with partial waves up to $J = 8$ in the Hartree-Fock and $J = 4$ in the dispersive contributions to the self-energy.

III. MOMENTUM DISTRIBUTION OF ONE-COMPONENT NUCLEAR SYSTEMS

We start the discussion of the SCGF results by highlighting the effect of correlations on the momentum distribution in SNM. Interaction-induced correlations have a distinctive signature in the momentum distribution, removing strength at momenta below the Fermi surface and shifting it to high momenta. In addition to the correlations induced by the NN force, however, the SCGF momentum distribution is sensitive to the temperature of the system. As a matter of fact, thermal correlations produce a similar signature on the momentum distribution: low momenta are depopulated, whereas high momenta are thermally occupied. The amount of low-momentum depletion and high-momentum population, however, is significantly different for both types of correlations. One can distinguish between these two types of effects by comparing the fully correlated SCGF prediction with the free Fermi gas (FFG) results, which are sensitive only to thermal correlations [64]. To this end, in Fig. 1 we show $n(k)$ of SNM for Av18 and the FFG for $\rho = 0.16$ fm^{-3} at $T =$ 5 MeV (left panel) and 10 MeV (right panel). At the lower temperature, the Fermi-Dirac distribution of the FFG deviates very little from a step function, $\Theta(k_F - k)$, which describes the $n(k)$ of the FFG at zero temperature. At this temperature and density, one can conclude that the thermal effects are small in the deep interior of the Fermi sea. Thermal effects, however, modulate $n(k)$ close to the Fermi surface, which is no longer discontinuous at k_F. Temperature is also responsible for the fact that, even in this very degenerate regime, the contribution of the states below k_F to the density sum rule is only 86%. The remaining 14% corresponds to thermally populated states above k_F. For the correlated case, $n(k)$ is rather flat below k_F and it presents a sizable depletion [that we will later on characterize by $n(0)$]. With the comparison with the FFG, one can conclude that dynamical NN correlations are mainly responsible for the depletion. Due to these effects, the contribution to the density sum rule of the states below k_F is reduced to 75%, i.e., 10% of the strength is shifted to higher momenta due to NN correlations. Consequently, momentum components of the wave function above k_F are generated. The high-momentum tail in $n(k)$ at this density and temperature provides 52% of the total kinetic energy per particle, to be compared to the much smaller 25% in the FFG.

At a larger temperature (right panel), thermal effects do not only modify the FFG $n(k)$ around the Fermi surface, but they also produce a depletion deep inside the Fermi sea. The lowest momentum state is depopulated by a few percentages, $n(0) = 0.97$. The shape of $n(k)$ differs significantly from the step function, documenting the loss of degeneracy at this temperature and density, even though it is still far from the classical Boltzmann momentum distribution. The fraction of particles that occupy states below k_F in the FFG decreases to 73%, while they contribute only the 53% of the kinetic energy per particle. At this temperature, the momentum distribution of the correlated system deep inside the Fermi sea exhibits a depletion, $1 - n(0) = 15\%$, which is approximately the sum of the depletion associated with the dynamic NN correlations ($\sim$13%) plus the one coming from the thermal distribution of the FFG (3%). The high-momentum tail is, however, substantially more important in the correlated case and the fraction of particles in states above the Fermi momentum increases to 44%, while the contribution to the kinetic energy amounts to 56%.

The depletion of the momentum distribution below the Fermi surface can be taken as a measure of the importance of both thermal and dynamical correlations in many-body systems. In the degenerate regime, where thermal effects are unimportant, the amount of strength removed at low momenta is closely related to the structure of the underlying NN force and is particularly sensitive to the short-range core as well as to the tensor components. In the correlated case, the low-momentum region of the momentum distribution is rather flat and almost independent of momentum as long as the temperature is relatively low and the density is large enough. For high temperatures or low densities, $n(k)$ is softened by thermal correlations. One can therefore focus on the $k = 0$ state to discuss generic depletion effects in both regimes. Figure 2 displays the density dependence of the occupation of this state for SNM (left panel) and PNM (right panel). Results for the Av18 (CDBonn) interaction are shown in solid (dotted) lines,

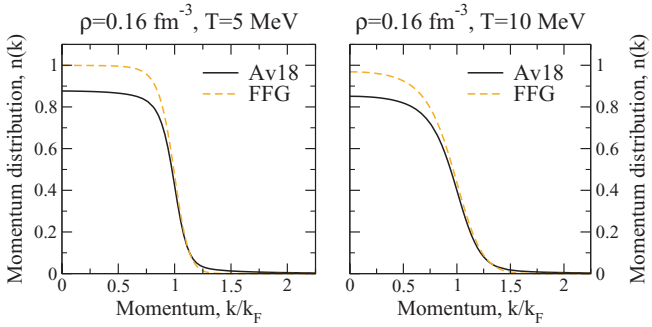

FIG. 1. (Color online) Correlated momentum distribution obtained with the Av18 interaction at $\rho = 0.16$ fm^{-3} and two temperatures: $T = 5$ MeV (left panel) and $T = 10$ MeV (right panel). The dashed line corresponds to the momentum distribution of the free Fermi gas under the same conditions.

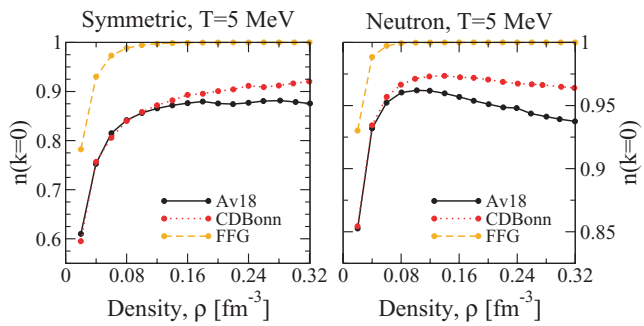

FIG. 2. (Color online) Density dependence of the occupation of the lowest momentum state at $T = 5$ MeV for Av18 (solid lines), CDBonn (dotted lines), and the FFG (dashed lines). The left (right) panel corresponds to nuclear (neutron) matter results. Note the different vertical scale of the two panels.

while dashed lines represent the FFG depletion under the same conditions.

The noninteracting depletion is extremely helpful in understanding the influence of thermal effects on the low-momentum components. At high densities, degeneracy dominates over temperature, and $n(0) = 1$ as expected from the zero temperature FFG momentum distribution. This degenerate regime determines the region where interaction-induced correlations represent the major contribution to the depletion in the correlated case. Consequently, the results obtained in this regime can be taken as faithful representatives of zero-temperature calculations. At lower densities, however, the FFG drops rapidly as density decreases, indicating that thermal effects dominate the low-momentum components of $n(k)$. The decrease observed in $n(0)$ for the correlated case should therefore be associated with temperature effects rather than with NN correlations. In this region, the correlated $n(0)$ yields interaction-independent results, as expected from the virial expansion [65] and illustrated in the figure. Note also that the onset density for the thermally dominated region is larger for symmetric matter ($\rho \lesssim 0.16$ fm^{-3}) than for neutron matter ($\rho \lesssim 0.08$ fm^{-3}). This corresponds to the notion that, for a given density, neutron matter is more "degenerate," i.e., has a larger Fermi momentum for the same value of ρ.

If we take the deviation of $n(0)$ from 1 as a measure of correlations, we can say that neutron matter is "less correlated," in general, than nuclear matter (note the different vertical scale of the two panels of Fig. 2). Moreover, the behavior of $n(0)$ as a function of density in the region where thermal effects are unimportant is very different for PNM and SNM. In neutron matter, as the density increases, the population of low momenta drops. This result agrees with the intuitive idea that, as particles are closer together on average, the effect of the short-range core increases and low-momentum strength is shifted to high momenta. Also in accordance with this picture, the depletion is more important for an interaction with a harder core (Av18) than for a softer force (CDBonn) [25]. In stark contrast, for SNM the opposite density dependence is observed: the depletion is constant or *decreases* as the density increases. For Av18, the depletion saturates at a constant value of $n(0) \sim 0.87$ as density increases, while for CDBonn a clear increase of $n(0)$ with density is observed.

What causes such a different behavior in the density dependence of $n(0)$? The major difference between neutron and nuclear matter lies in the role of the strong $^3S_1$-$^3D_1$ tensor component, which is only active in the latter. It appears that the effect of this component is twofold. On the one hand, it increases, in general, the depletion as compared to the effect of short-range correlations by themselves, as seen by comparing SNM and PNM results. On the other hand, tensor components seemingly modify the density dependence of $n(0)$. This nontrivial result requires a deeper understanding for which the Green's functions formalism offers a unique perspective by connecting directly the momentum distribution and the in-medium self-energy, as will be discussed in Sec. IV. Suffice it to say for now that the effect of the tensor force is not only limited to the depletion low-momentum components but is also responsible in higher order for binding effects, as illustrated by the deuteron.

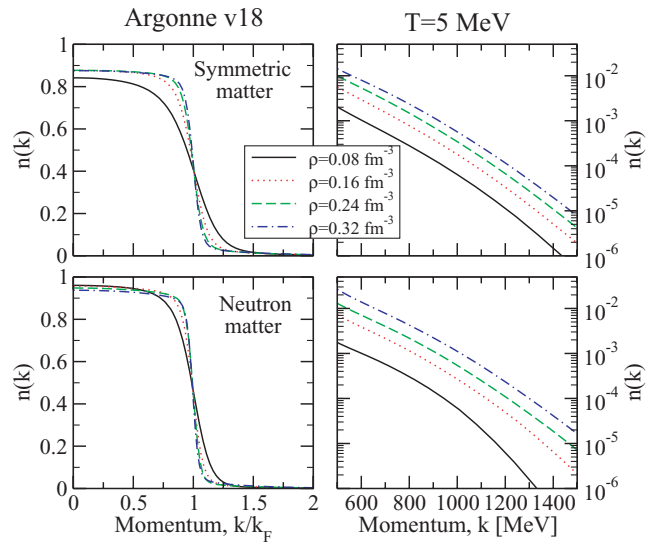

FIG. 3. (Color online) Momentum distribution of symmetric (upper panels) and neutron (lower panels) matter obtained with the Av18 interaction at $T = 5$ MeV for different densities. The right panels focus on the high-momentum region.

The normalization of the momentum distribution to the total density, Eq. (33), forces the missing strength at low momentum to be shifted to high-momentum states. The shift in strength may depend on the physical properties of the system (temperature, density, isospin content). Figure 3 shows the momentum distribution of symmetric (upper panels) and neutron (lower) matter for Av18. In all cases the temperature is 5 MeV and four different densities are displayed. In the left panels the momentum distribution is displayed as a function of the ratio k/k_F, where $k_F = (6\pi^2/\nu\rho)^{1/3}$ is the Fermi momentum of the system. This allows for a clear inspection of the density dependence of $n(k)$ and can be instructive in understanding the scaling of the distribution as a function of density. At a constant temperature, an increase in density leads to a more degenerate system. Consequently, the high density results have a more zero-temperature-like structure, with an almost constant depletion below k_F and a substantial jump in $n(k)$ at $k = k_F$. In contrast, at low densities, the momentum distribution is modulated by temperature at all momenta. Comparing the four different densities, one can observe that one major density effect is the redistribution of strength in the region close to the Fermi surface. Note that on the present scale the effects on the depletion shown in Fig. 2 are hard to see. In general, though, Av18 leads to a saturation of the depletion in symmetric matter and to a decrease of the population of low momenta for high-density neutron matter.

The high-momentum components are shown in the right panels of Fig. 3 on a logarithmic scale for momenta ranging between 500 and 1500 MeV. In both symmetric and neutron matter, the high-density results lead to a larger population of high-momentum states. This is in contrast to the low-momentum states, which exhibit a very different density dependence for the two cases. All in all, this suggests that the mechanism that produces high-momentum components only scales with density and is rather momentum independent.

There have been suggestions in the literature that high-momentum components scale with k_F^5 as a function of density. Such results have been obtained for a separable version of the Paris interaction [15] and a central (no tensor effects) version of the Reid soft-core interaction [66]. These interactions have a stronger core, which may explain the different behavior. In addition, in the limit of extremely dilute matter, the high-momentum components scale with k_F^6 for the hard-sphere Fermi gas [67]. Our calculations, based on more recent, softer realistic interactions, scale more like k_F^3 [30].

IV. RELATION OF $n(k)$ TO THE TIME-ORDERED SELF-ENERGY

The Green's functions method is unique in that it can provide an interpretation of the previous results in terms of the *sp* spectral function. The interplay between thermal and density effects in $n(k)$ can be qualitatively understood in terms of the evolution in temperature and density of both the spectral function and the phase-space distribution [see Eq. (28)] [31]. Unfortunately, it is not straightforward to go beyond this sort of reasoning and find a simple connection to the in-medium interaction. A different perspective and additional insight can be achieved by considering an approximate relation between the momentum distribution and the components of the time-ordered self-energy. The analysis will be performed for $T = 0$ to make contact with earlier work on this subject [66,68–71]. Let us write the Dyson equation at $T = 0$ in the form

$$\mathcal{G} = \mathcal{G}^0 + \mathcal{G}^0\Sigma\mathcal{G} = \sum_{n=0}^{\infty} \mathcal{G}^0\{\Sigma\mathcal{G}^0\}^n, \tag{35}$$

where $\mathcal{G}^0$ is the *time-ordered* noninteracting *sp* propagator. The momentum distribution can then be written as

$$\begin{aligned} n(k) &= \int_C \frac{d\omega}{2\pi i}\mathcal{G}(k,\omega) \\ &= \int_C \frac{d\omega}{2\pi i}\sum_{n=0}^{\infty}\mathcal{G}^0\{\Sigma\mathcal{G}^0\}^n. \end{aligned} \tag{36}$$

with C representing a contour composed of the real axis and closed by a semicircle in the upper half-plane. To proceed it is necessary to decompose the self-energy into its different time-ordered contributions

$$\begin{aligned} \Sigma(k,\omega) &= \Sigma_{\rm HF}(k) + \Sigma_{\downarrow}(k,\omega) + \Sigma_{\uparrow}(k,\omega) \\ &= \Sigma_{\rm HF}(k) - \int_{\varepsilon_F}^{\infty}\frac{d\omega'}{\pi}\frac{{\rm Im}\Sigma_{\downarrow}(k,\omega')}{\omega_+ - \omega'} \\ &\quad + \int_{-\infty}^{\varepsilon_F}\frac{d\omega'}{\pi}\frac{{\rm Im}\Sigma_{\uparrow}(k,\omega')}{\omega_- - \omega'}. \end{aligned} \tag{37}$$

The first term in the expansion of Eq. (36), corresponding to $\mathcal{G}^0$, yields the step function momentum distribution, $n^0(k) = \Theta(k_F - k)$, of the FFG. Using Eq. (37), the second term ($n = 1$) in Eq. (36) yields three contributions, each of them with two noninteracting propagators, $\mathcal{G}^0$. For $k < k_F$, the contribution with the Hartree-Fock term vanishes on account of the double pole inside the contour, which leads to the derivative of a constant when Cauchy's integral formula is applied. The contribution with $\Sigma_{\uparrow}$ can be shown to be zero as well by using the corresponding dispersion relation for $\Sigma_{\uparrow}$ and applying the residue theorem (the residues cancel). Only the term with $\Sigma_{\downarrow}$ finally contributes and yields:

$$n^1_{\uparrow}(k) = \partial_{\omega}{\rm Re}\Sigma_{\downarrow}(k,\omega)|_{\omega=\varepsilon^0(k)}, \quad k < k_F, \tag{38}$$

by applying Cauchy's integral formula. The derivative is applied at the pole of the noninteracting propagator. Because the peak of the dressed propagator will normally occur at the quasiparticle energy

$$\varepsilon(k) = \frac{k^2}{2m} + {\rm Re}\Sigma[k,\varepsilon(k)], \tag{39}$$

it is convenient to include an auxiliary potential

$$U(k) = {\rm Re}\Sigma[k,\varepsilon(k)], \tag{40}$$

anticipating that the derivative in Eq. (38) must be taken at the location where most of the *sp* strength is concentrated. This leads to an additional constant term in Eq. (37), where U must be subtracted. An approximate result for $n(k)$ for $k < k_F$ can now be obtained by expanding $\Sigma_{\downarrow}$ only up to first order at $\varepsilon(k)$ in all contributions to higher-order terms ($n > 1$) in Eq. (36). This approximation will therefore be best for momenta as far as possible from the Fermi energy, because from the corresponding dispersion relation it is clear that a linear approximation to the energy dependence will be most appropriate for $k = 0$ [for which $\varepsilon(0)$ is farthest from ε_F]. The series with only $\Sigma_{\downarrow}$ terms yields

$$n_{\uparrow}(k) = \frac{1}{1 - \partial_{\omega}{\rm Re}\Sigma_{\downarrow}(k,\omega)|_{\omega=\varepsilon(k)}}, \quad k < k_F, \tag{41}$$

because a geometric series is produced with the energy derivative appearing in each higher order. Other terms including the constant $\Sigma_{\rm HF}$ and $\Sigma_{\uparrow}$ will not contribute in a similar fashion as in the term with $n = 1$, as long as the validity of this expansion for $\Sigma_{\downarrow}$ is assumed.

For momenta above k_F, the noninteracting propagators in Eq. (36) have poles outside the contour C and cannot contribute. Only terms with the derivative of $\Sigma_{\uparrow}$ will occur when a similar expansion as for $k < k_F$ is employed. The $n = 1$ term accordingly generates the first contribution to $n(k)$ for $k > k_F$, given by

$$n^1_{\downarrow}(k) = -\partial_{\omega}{\rm Re}\Sigma_{\uparrow}(k,\omega)|_{\omega=\varepsilon(k)}, \quad k > k_F. \tag{42}$$

For high momenta this will be the dominant contribution to $n(k)$, because the location of $\varepsilon(k)$ can be quite far from ε_F. Summing the geometric series from higher-order contributions with $\Sigma_{\uparrow}$ (with the approximation of keeping only linear terms in the energy) then yields

$$n_{\downarrow}(k) = 1 - \frac{1}{1 - \partial_{\omega}{\rm Re}\Sigma_{\uparrow}(k,\omega)|_{\omega=\varepsilon(k)}}, \quad k > k_F. \tag{43}$$

While Eqs. (41) and (43) have not been rigorously derived here, we note that these results have been employed before in the literature [70]. Indeed, it turns out that their numerical implementation generates an accurate approximation to the full result for $n(k)$, except in the immediate vicinity of the Fermi surface, as will be illustrated in the following. Moreover, these equations allow for a deeper understanding of the

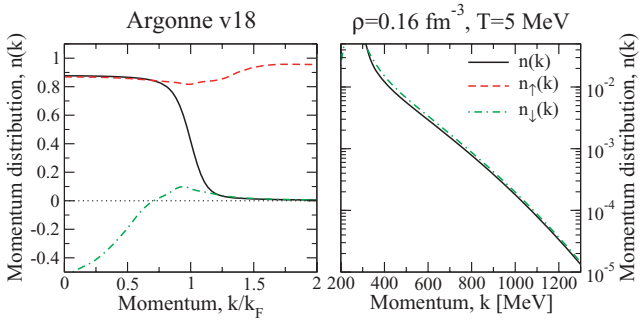

FIG. 4. (Color online) Correlated momentum distribution obtained with the Av18 interaction at $\rho = 0.16$ fm^{-3} and $T = 5$ MeV (solid line). The $n_\uparrow(k)$ and $n_\downarrow(k)$ contributions of Eqs. (41) and (43) are shown in dashed and dot-dashed lines, respectively.

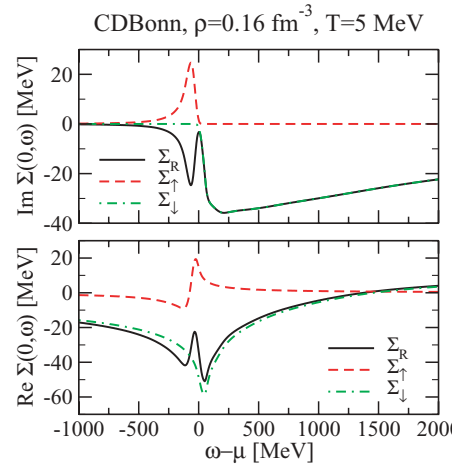

FIG. 5. (Color online) Different components to the imaginary (upper panel) and real (lower panel) parts of the self-energy for CDBonn at $\rho = 0.16$ fm^{-3} and $T = 5$ MeV.

observed trends in the depletion of the Fermi sea. Because the decomposition of the self-energy in terms of "up" and "down" components is essential for this derivation, it clarifies the need for introducing these terms also at finite temperature.

For a self-consistent calculation at finite temperature, expressions (41) and (43) reproduce the momentum distribution obtained from the complete spectral function extremely well in their respective momentum range. An example is shown in Fig. 4 for Av18 at $\rho = 0.16$ fm^{-3} and $T = 5$ MeV. The hole contribution coming from Eq. (41) (dashed line, left panel) is a very good approximation to the momentum distribution for momenta below $0.75k_F$. Similarly, for momenta above $1.25k_F$, $n(k)$ is very well approximated by Eq. (43) (dash-dotted line, right and left panels). A similar agreement is found in a wide range of densities and temperatures and also for other NN forces. We note that, for these results to be valid, it is essential to calculate the derivatives at the corresponding quasiparticle energies and therefore self-consistency is a necessary ingredient in obtaining this good agreement.

Having found a direct connection between $n(k)$ and the self-energy, one can try to establish a relation between the density dependences of $n(k)$ and the density and energy dependence of the self-energy. To this end, let us discuss the structure of $\Sigma_\uparrow$ and $\Sigma_\downarrow$. Figure 5 shows the self-energy of the $k = 0$ state as a function of energy for the CDBonn potential at $\rho = 0.16$ fm^{-3} and $T = 5$ MeV. The upper panel displays three different components of Σ. The solid line corresponds to the retarded self-energy, which has traditionally been used and discussed in finite-temperature SCGF calculations [30,44]. Note that $\mathrm{Im}\Sigma_\mathcal{R}$ is negative at all energies and displays two distinctive peaks: a relatively small peak in the "hole" region, $\omega < \mu$, and a much larger structure in the "particle" region, $\omega > \mu$. While the hole components decay rapidly for negative energies, the particle side has a much slower decay in energy due to the combination of the large particle-particle phase-space and short-range correlation effects, in complete analogy with earlier results obtained for $T = 0$ [46].

Because the self-energy has the same analytical structure as the sp propagator, the time-ordered contributions of Σ can be obtained from the retarded component by using equivalent expressions to Eqs. (20) and (21). The phase-space factors in the imaginary parts isolate the respective particle and hole regions. Consequently, $\mathrm{Im}\Sigma_\uparrow$ and $\mathrm{Im}\Sigma_\downarrow$ have a single peak below and above the Fermi surface, respectively. In the case of the hole contribution, the peak has the opposite sign compared to the retarded component, but for the particle one it coincides with the $\mathrm{Im}\Sigma_\mathcal{R}$ peak. The differences between the retarded and the corresponding time-ordered imaginary components will be larger in the $\omega \sim \mu$ region, due to the variation of the thermal distribution in this region. In particular, at higher temperatures, the opening of phase space can eventually lead to the appearance of additional peaks in the self-energy of each component, due to the overlap between the "opposite" peak and the nonzero Fermi-Dirac distribution.

The different imaginary components of Σ are related to their respective real parts by the dispersion relations of Eqs. (14), (17), and (19). These real parts are illustrated in the lower panel of Fig. 5. The important consequences of the isolation of the hole and particle components in the imaginary part can be clearly observed now. $\mathrm{Re}\Sigma_\uparrow$ decays rapidly at low and high energies, because the hole strength in the imaginary part is limited to a relatively narrow energy domain. This component exhibits a wiggle at small negative energies, associated with the hole peak. The down component of Σ has a substantial contribution at all energies, as a consequence of the extremely long energy tail of the imaginary part [25,30,31]. It also has a peak structure, related to the onset of a very fast decrease of $\mathrm{Im}\Sigma_\downarrow$ near $\omega \sim \mu$. This threshold, together with the relatively large and constant energy tail, are at the origin of a bell-shaped minimum. As we shall see in the following, it is this minimum that dominates the low-energy components of the momentum distribution. The real part of the down component has a zero at high energies, $\sim$1.5 GeV, and it is still substantial at very high energies. These results are in good qualitative agreement with the zero-temperature calculations of Ref. [46] for a much harder interaction.

The decomposition of Σ in its time-ordered components can also be used to better understand the structure of the retarded self-energy. The sum of $\mathrm{Re}\Sigma_\uparrow$ and $\mathrm{Re}\Sigma_\downarrow$ must coincide with the real part of the retarded self-energy [42]. The high positive and negative energy tails of the retarded self-energy have to

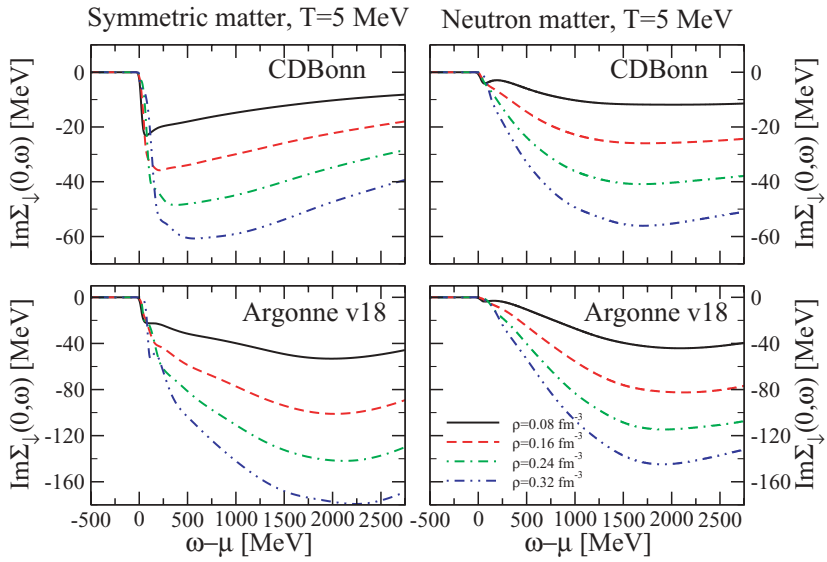

FIG. 6. (Color online) Imaginary part of $\Sigma_\downarrow$ as a function of energy for the $k = 0$ state. Different densities are displayed with different line styles. The upper panels have been obtained with CDBonn, whereas the lower panels correspond to Av18. Symmetric (neutron) matter results are shown in the left (right) panels. Note the difference in scales between the upper and lower panels.

be related to the down component of Σ, which is the only active contribution in these regions. Moreover, the double-peak structure of $\mathrm{Re}\Sigma_\mathcal{R}$ at $\omega \sim \mu$ is caused by the superposition of the up and down peaks and wiggles in this region. In particular, the $\omega < \mu$ peak in $\mathrm{Re}\Sigma_\mathcal{R}$ is a reflection of the negative side of the wiggle in $\mathrm{Re}\Sigma_\uparrow$, while the $\omega > \mu$ peak is mostly due to the down component. The relative importance of the hole and particle peaks changes with momentum, with the "particle" side becoming more prominent as k increases. In spite of this important shift, the connection between the up and down components and the high energy and peak structures of the retarded self-energy remains valid.

The $\Sigma_\downarrow$ self-energy is related, via Eq. (41), to the momentum distribution below k_F. This suggests that the density dependence of the low-momentum components of $n(k)$ can be understood in terms of the self-energy. Let us focus for simplicity on the $k = 0$ state. Figure 6 displays the energy dependence of $\mathrm{Im}\Sigma_\downarrow$ for different densities in the case of symmetric (left panels) and neutron matter (right panels). The upper (lower) panels correspond to the CDBonn (Av18) interactions. The imaginary part of $\Sigma_\downarrow$ has a very large structure in the $\omega > \mu$ region that only decays at extremely high energies. The area covered by this function depends substantially on the density, the NN potential and the isospin content of the system. In the high-energy regime, $\mathrm{Im}\Sigma_\downarrow$ displays a linear dependence in density for both nuclear and neutron matter.

A significant difference is found by comparing upper and lower panels in Fig. 6: the amount of imaginary part shifted to high energies is substantially larger for Av18 than for CDBonn (note the very different vertical scales). The down component of the self-energy is therefore very sensitive to the structure of the underlying NN force. This result suggests that hard interactions produce a much larger imaginary part than soft ones do [25], for both SNM and PNM. For a given NN interaction, however, the peak of $\mathrm{Im}\Sigma_\downarrow$ at high energies is relatively similar for the two systems, as seen by comparing left and right panels. While in PNM the peak can be attributed basically to short-range correlations, SNM has an additional contribution coming from the tensor components that generates an important imaginary part below 1000 MeV, as discussed in Refs. [11,72]. It is good to remember that the presence of an imaginary part in the self-energy above the chemical potential is directly responsible for the appearance of sp strength at those energies for momenta below k_F. In nuclear matter, the additional $^3S_1$-$^3D_1$ coupled channel with both its short-range and tensor contribution is thus responsible for the stronger and more pronounced imaginary part starting above the chemical potential as compared to neutron matter, where it is absent. The position of the peak in $\mathrm{Im}\Sigma_\downarrow$ also changes when going from symmetric to neutron matter but in an interaction-dependent way. While for CDBonn the peak is shifted to high energies for neutron matter, the contrary happens for Av18 [25].

The energy dependence of the imaginary part has an immediate impact on the real part of $\Sigma_\downarrow$ by means of the dispersion relation. Figure 7 shows this component in a narrower energy range for various densities. In general, the real part is proportional to the density, with higher densities leading to more attractive real self-energies (in the range displayed in the figure). Comparing left and right panels, one observes an important difference between symmetric and neutron matter. Although a distinctive inverted peak develops in nuclear matter for the two NN interactions, in neutron matter only a very broad minimum is observed. The origin of this peak is associated with the rapid drop, from zero to negative values, of $\mathrm{Im}\Sigma_\downarrow$ in a narrow energy band around $\omega \sim \mu$. This sharp threshold occurs for symmetric matter (see the upper left panel of Fig. 6, for instance), but it is not as sharp in neutron matter, reflecting the important on/off role of the tensor force in these systems. As a consequence of these large differences, the dispersive counterparts of the threshold of the imaginary part are very different for both systems.

The presence of the inverted peak in symmetric matter has important consequences for the momentum distribution at low momenta. To compute $n(k)$, the partial derivative with respect to the energy of $\mathrm{Re}\Sigma_\downarrow$ is computed at the quasiparticle peak. The quasiparticle energy for $k = 0$ at different densities is identified by dots in Fig. 7. As expected, at zero momentum the quasiparticles are more bound for higher densities, so

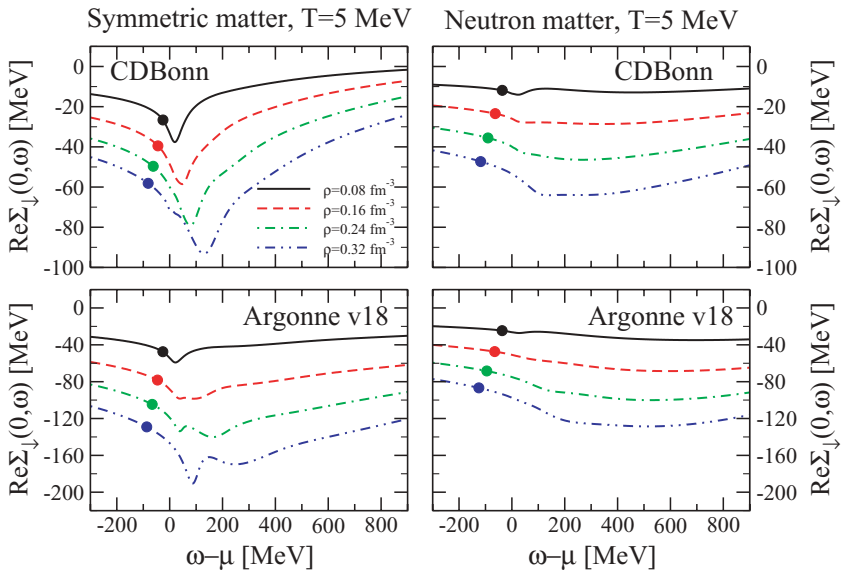

FIG. 7. (Color online) The same as Fig. 6 for the real part of $\Sigma_\downarrow$. The dots represent the position of the quasiparticle peak.

their energies shift to more negative values with respect to the chemical potential. In SNM, this shift moves the quasiparticle contribution further away from the inverted peak, which is displaced to higher energies as density increases. The combination of the two effects (attractive quasiparticle shift, repulsive peak shift) is such that the slope at the quasiparticle energy is reduced with increasing density. For PNM, the quasiparticle shift is larger, but the inverted peak is absent and the broad structure is such that the local slope around the quasiparticle contribution decreases with density.

To clarify these issues, we show in Fig. 8 the partial derivative with respect to the energy of the self-energy at $T = 5$ MeV for different densities. Upper (lower) panels correspond to symmetric (neutron) matter, while left (right) panels show results for Av18 (CDBonn). Let us first focus on the SNM case (upper panels). At all densities, the inverted peak in the real part (a zero in the derivative) lies inside the $\omega > \mu$ region, and it is therefore not visible in the figure. Instead, we have chosen to display the $\omega < \mu$ regime, where the derivative should be taken according to Eq. (41). This corresponds to the wings of the peak on the left side. At these energies, the slope of $\mathrm{Re}\Sigma_\downarrow$ decreases with energy and, in general, has more negative values at higher densities. The increase of the slope with density also appears to be related to the hardness of the interaction. While for CDBonn the slope changes very little as density increases, Av18 leads to much larger variations in SNM. The soft interaction, therefore, generates a small variation in density of $\partial_\omega \mathrm{Re}\Sigma_\downarrow$ which, together with the quasiparticle shift, produces a *decreasing* depletion as the density increases. This observation therefore explains the counterintuitive behavior observed in the left panel of Fig. 2. For a harder interaction, such as Av18, the effect of density in the slope is much larger, while the quasiparticle shift is similar to CDBonn. Consequently, there is the possibility for the depletion to saturate (or even decrease) at high densities. Earlier results for a separable version of the Paris potential exhibit little density dependence for the depletion [15] not unlike our results for Av18 in the range from once to twice normal density. Note that

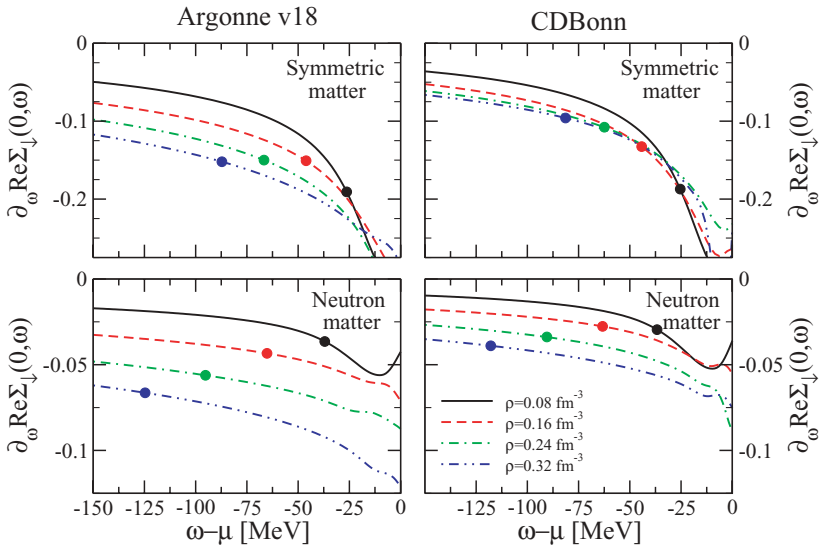

FIG. 8. (Color online) Partial derivative of $\Sigma_\downarrow$ as a function of energy for the $k = 0$ state at $T = 5$ MeV. Different densities are displayed with different line styles. The upper panels show symmetric matter results, while the lower panels correspond to neutron matter. Left (right) panels have been obtained with the Av18 (CDBonn) interaction.

the density dependence of the self-energy is closely related to the strong correlation effects induced by the short-range components.

The density dependence of the partial derivative is also important in neutron matter (lower panels). Again, the slope changes much more as a function of density for Av18 than for CDBonn. Due to the quasiparticle shift, the derivative at zero momentum decreases. Thus, the depletion increases with density, in agreement with the right panel of Fig. 2. For a given NN interaction, the overall decrease of $\partial_\omega \mathrm{Re}\Sigma_\downarrow$ with density and the quasiparticle shift are qualitatively similar for both neutron and nuclear matter. The origin of the differences between SNM and PNM should thus be attributed to the energy dependence of the slope, which is much more pronounced for symmetric matter than for neutron matter. This is particularly true for energies close to $\omega \sim \mu$, where a sharp decrease is observed associated with the inverted peak in the real self-energy. As we have already discussed, this is largely related to the threshold behavior of the imaginary part of $\Sigma_\downarrow$. In turn, this behavior must be partly ascribed to the tensor component of the one-pion-exchange interaction.

V. MOMENTUM DISTRIBUTION OF TWO-COMPONENT NUCLEAR SYSTEMS

Up to now, we have considered the momentum distributions for two extreme cases, namely SNM and PNM. It is also illustrative to study the dependence of the proton and neutron momentum distributions, $n_\tau(k)$, as a function of the asymmetry parameter, α. This analysis should shed some light on the isospin dependence of single-particle nuclear properties coming from volume effects. In particular, tensor effects can be highlighted in asymmetric systems and can be pinpointed by a comparison of different NN potentials.

The asymmetry dependence of the neutron- and proton-momentum distribution is presented in Fig. 9 at $\rho = 0.16$ fm^{-3} and $T = 5$ MeV. The left (right) panel contains the results for FFG (Av18). For $\alpha = 0$ (symmetric case), the momentum

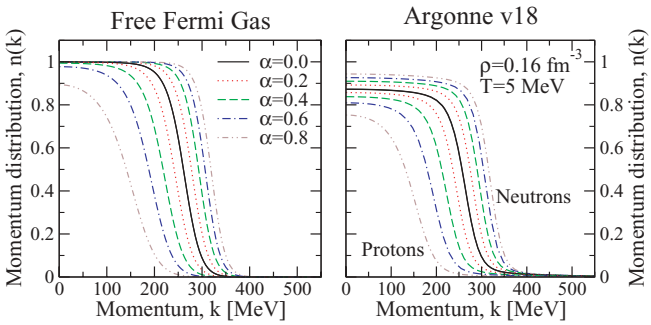

FIG. 9. (Color online) Isospin asymmetry dependence of the free Fermi gas (left panel) and the correlated momentum distribution from Av18 (right panel). The density ($\rho = 0.16$ fm^{-3}) and temperature ($T = 5$ MeV) are fixed and the results for different asymmetries are shown in different line styles. Symmetric matter results correspond to the central solid curve, while curves to its right (left) correspond to neutron (proton) distributions for the corresponding isospin asymmetric cases.

distributions of neutrons and protons coincide in both cases. Let us discuss first the left panel, where we show the momentum distribution of the isospin asymmetric FFG. For the symmetric case ($\alpha = 0$) and as discussed previously in the context of Fig. 1, the thermal effects on $n(k)$ are visible only at the Fermi surface and almost no depletion occurs inside the Fermi sea. The same is true for the most abundant component as asymmetry increases: the depletion is negligible and the Fermi momentum is displaced to larger values. For protons, however, $n(k)$ is clearly affected by temperature, exhibiting a large change in shape in a wide region of momenta. At large asymmetries, in particular, the momentum distribution of the less abundant components differs substantially from the step function, losing its degeneracy character and decreasing the occupation at the origin. In some sense, when increasing the asymmetry, the less abundant component moves closer to a classical momentum distribution, while the most abundant component becomes more degenerate. Note, however, that, at $\alpha = 0.8$, one is still far away from the classical regime even though thermal effects are important. This analysis suggests that one should take into account thermal corrections when analyzing the change in asymmetry of $n_\tau(k)$ also for the correlated case.

Focusing on the right panel, one observes that the most abundant component (neutrons for positive α) gets less depleted when the asymmetry increases, i.e., neutrons become "less correlated." This is in contrast to the FFG results, which, for neutrons, exhibit no change inside the Fermi sea. The decrease of depletion for the most abundant component in this density and temperature should be taken as a pure NN correlation effect. This behavior can be explained in simple terms as follows. Although the total number of pairs is the same when increasing the asymmetry at constant density, some of the pn pairs are replaced by neutron-neutron pairs. The latter correlations are weaker than the pn ones, due to the absence of tensor effects, and therefore neutrons become less correlated at large α's. Conversely, the momentum distributions of the less abundant species (protons) become more depleted with asymmetry. A single proton sees an increasing number of neutrons when the asymmetry increases, i.e., pp pairs are replaced by the more correlated pn pairs, which results into a more depleted proton momentum distributions. Together with this, protons "feel" more the effect of temperature. The proton density in the asymmetric system decreases as α increases. At finite temperature, this is translated into the fact that $n_p(k)$ becomes dominated by thermal effects at large asymmetries and looks less degenerate. The plateau associated with hole states, for instance, which is clearly observed for neutrons at all asymmetries, gets washed out for protons at large α. Consequently, one should be careful in associating the increase of the depletion of protons only to dynamical NN correlation, because the momentum distribution of the less abundant component might be strongly influenced by thermal effects.

The information about the isospin dependence of the depletion is summarized in Fig. 10, where $n_\tau(0)$ is plotted as a function of the asymmetry at $T = 5$ MeV for $\rho = 0.16$ fm^{-3} (left panel) and $\rho = 0.32$ fm^{-3} (right panel). The FFG (dashed lines) results are compared to the Av18 (solid lines) and

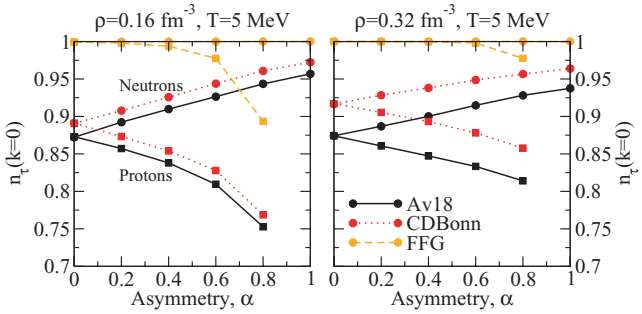

FIG. 10. (Color online) Isospin asymmetry dependence of the neutron (filled circles) and proton (squares) lowest momentum occupation. Correlated results for the Av18 (solid lines) and CDBonn (dotted lines) interactions are compared to the free Fermi gas (dashed lines) predictions.

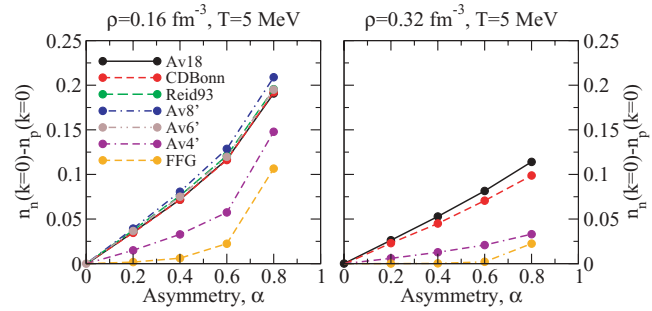

FIG. 11. (Color online) Difference of neutron and proton occupation of the lowest momentum state as a function of isospin asymmetry for different interactions. The two panels show results at $T = 5$ MeV for $\rho = 0.16$ fm^{-3} (left) and $\rho = 0.32$ fm^{-3} (right).

CDBonn (dotted lines) SCGF predictions. Again, the FFG results provide a measure of thermal effects. On the one hand, the occupation of the most abundant component at zero momentum does not change when the asymmetry increases, indicating that this species is totally degenerate in the whole range of asymmetries. On the other hand, the corresponding occupation of protons (the less abundant component) is close to 1 at small asymmetries and decreases as the asymmetry increases. At $\rho = 0.16$ fm^{-3}, this accounts for a $\sim$2% effect for $\alpha = 0.6$ and a $\sim$11% for $\alpha = 0.8$. As a matter of fact, in the limit $\alpha \to 1$, the protons become an impurity gas in a Fermi sea of neutrons, thus behaving as a classical gas with $n_p(0) \to 0$. The steepness of the change in $n_p(0)$ depends on the total density and the temperature of the system. At a higher density (right panel), the thermal effects affecting protons do not set in unless the asymmetry is very large and, even at $\alpha = 0.8$, the effect is only of $\sim$2%. Let us stress the fact that this is a pure thermal effect: for the FFG at zero temperature, $n_\tau(0) = 1$ for both protons and neutrons at all asymmetries.

For the correlated depletion, the occupation of the zero momentum state is an increasing (decreasing) function of the asymmetry for the most (less) abundant component. The behavior is very similar for both NN interactions, although the occupations for Av18 are systematically smaller than those for CDBonn at both densities. The differences between the two potentials increase with density (see right panel). The comparison with the FFG allows us to identify the regime in which NN correlations dominate over thermal effects. At $T = 5$ MeV and $\rho = 0.16$ fm^{-3}, for instance, and up to asymmetries of about $\alpha \sim 0.4 - 0.6$, the occupations of neutrons and protons can be attributed to dynamical correlations and should provide a good estimate for the case of zero temperature. Up to these asymmetries, both the neutron and the proton depletion change almost linearly with asymmetry. In the left panel, the depletion of protons starts to bend down for larger asymmetries, attributable to the onset of thermal effects. In a more degenerate case (right panel), where thermal effects are almost negligible, the asymmetry dependence of both $n_\tau(0)$'s is again found to be linear.

Asymmetries of stable nuclei belong to the lower range of asymmetries, i.e., $\alpha \sim 0.2$ for ^{208}Pb. The SCGF predictions should be valid in this range, where thermal effects are unimportant. Unfortunately, the difference between the occupation of protons at this asymmetry and the symmetric case is only $\sim$2%, too small to allow experimental verification. Nuclei at larger asymmetry produced at future rare isotope facilities may provide a better testing ground. Moreover, integrated effects over the whole neutron and proton density profiles might also enhance the effect of asymmetry. Let us note that, for finite nuclei, one should also take into account surface properties and their isospin dependence. In particular, an asymmetry dependent effect associated with surface properties has been identified for protons in Ca isotopes [36,37].

A surprising feature arises when comparing the two panels of Fig. 10. In spite of the differences observed in both SNM and PNM for the Av18 and CDBonn results, the asymmetry dependence of $n_\tau(0)$ is very similar at all densities. This is shocking because, as we have stressed so far, both forces have a rather different short-range behavior and tensor structure. Given the almost linear dependence of $n_\tau(0)$ with asymmetry, a better insight into these differences can be gained by plotting the difference $n_n(0) - n_p(0)$. In Fig. 11, we present this "iso-depletion" for different interactions as a function of the asymmetry at $T = 5$ MeV for the same densities as before. The left panel shows that this difference is the same for a wide variety of modern NN potentials, independently of their short-range or operatorial structure. This seems to suggests that the iso-depletion is fixed by the phase shifts, most probably via their isospin dependence. This is corroborated at higher densities by comparing the very similar Av18 and CDBonn predictions (right panel).

In both panels, there are two results that fall below the main iso-depletion line. Immediately below most of the interactions, one finds the results corresponding to the Av4′ potential. This has an extremely simplified operatorial structure, with only a spin-isospin part and no tensor components, and is fitted to reproduce the binding energy of the deuteron [62]. The fact that it lies significantly below the other results shows the importance of tensor effects for isospin asymmetric systems. It appears that the tensor force tend to increase the difference between neutron and proton momentum distributions as asymmetry increases. Moreover, the comparison with Av6′ and Av8′ suggests that, once the tensor components are included in a force, the iso-depletion will remain almost the same

TABLE I. Occupation of the lowest momentum state for different NN interactions in symmetric and neutron matter.

Interaction	Symmetric	Neutron
CDBonn	0.891	0.972
Reid93	0.872	0.962
Argonne v18	0.872	0.957
Argonne v8′	0.863	0.956
Argonne v6′	0.879	0.964
Argonne v4′	0.946	0.971
FFG	0.9993	0.999991

independently of the extra spin-orbit terms. Let us again stress the fact that such an agreement for different potentials is very surprising, particularly if one considers the fact that the momentum distributions of neutrons and protons can be different for each potential.

The FFG iso-depletion is, in all the cases explored, below the correlated results, which shows the importance of NN interaction-induced effects. Let us note that the effect of beyond mean-field correlations is essential in this case. Mean-field calculations, either with realistic or phenomenological forces, will predict results of the same order of magnitude of the FFG. Again, the latter provides a measure of thermal effects. In the left panel, for instance, the correlated iso-depletion at the largest asymmetry considered should be significantly affected by thermal effects and therefore one should not take that value as a NN dynamical correlation effect. For the right panel, thermal effects are suppressed by degeneracy and the results can be taken as purely interaction-induced, zero-temperature values.

Table I summarizes the values of $n(0)$ for SNM and PNM at $\rho = 0.16$ fm^{-3} and $T = 5$ MeV for the different interactions considered in the left panel of Fig. 11. In all cases, $n(0)$ for PNM is larger than for SNM, confirming the notion that, for the same density, neutron matter is less correlated than nuclear matter. The values of the depletion for both systems are within less than 5% of each other for the three phase-shift equivalent potentials (and also for Av6′ and Av8′), which suggests that this quantity is rather well established at the theoretical level. Numerical uncertainties are well under control in this case and will only affect the third significant digit in the correlated calculations. Moreover, the difference of the occupation between neutron and nuclear matter is rather constant for all potentials. The conclusion is therefore warranted that the asymmetry dependence of the difference between the depletion for neutrons and protons is rather strongly constrained once an interaction is employed that yields an accurate description of the NN phase shifts. Av4′ does not reproduce these and produces an unrealistically small depletion for SNM, thus effectively decreasing the difference between nuclear and neutron matter. Due to the fact that both neutron and nuclear matter are degenerate systems at this density and temperature, as indicated by the extremely small depletions for the FFG case, these results are not affected by thermal effects. As a matter of fact, the results obtained with Reid93 are in very good agreement with previous calculations at zero temperature for the same potentials, obtained with a different procedure to implement the SCGF method [47].

The isospin asymmetry dependence of $n_\tau(0)$ can also be analyzed in terms of the time-ordered components of the self-energy. Figure 12 shows the $k = 0$ imaginary (left panels) and real (central panels) parts of $\Sigma_\downarrow$, at $\rho = 0.16$ fm^{-3} and $T = 5$ MeV, as a function of the energy for different asymmetries. Upper (lower) panels display the results for neutrons (protons) obtained for the Av18 interaction. The increase of isospin asymmetry has a repulsive effect in the neutron Im$\Sigma_\downarrow$, which

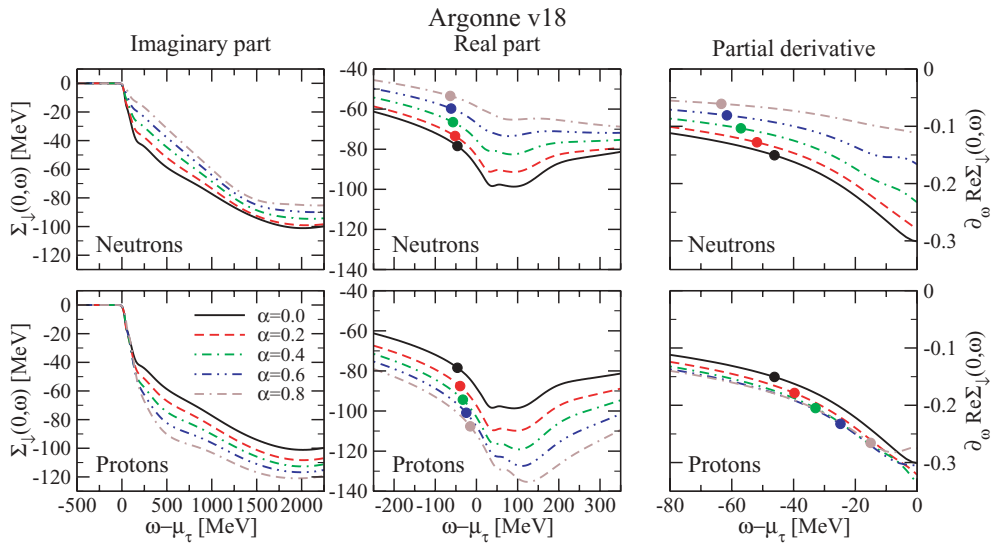

FIG. 12. (Color online) The $k = 0$ imaginary (left panels) and real (central panels) parts of $\Sigma_\downarrow$ as a function of the energy for different asymmetries at $\rho = 0.16$ fm^{-3} and $T = 5$ MeV. Upper (lower) panels display the results for neutrons (protons) obtained from the Av18 interaction. The right panels display the partial derivatives of the real part with dots representing the location of the self-consistent quasiparticle energy.

is shifted by almost a constant amount as α increases. The minimum in this function becomes shallower and the threshold at $\omega \sim \mu_\tau$ is less pronounced. These repulsive effects are associated with the decreasing importance of the tensor force for neutrons with increasing asymmetry. As a consequence of the diminishing threshold behavior, the inverted peak in $\mathrm{Re}\Sigma_\downarrow$ for neutrons is smeared out at large α's. The corresponding partial derivatives (right panels) become smaller in absolute value and, together with the quasiparticle shift, lead to a decrease of neutron depletion as asymmetry increases. Let us note here that the $k = 0$ quasiparticle energies for neutrons become more repulsive as asymmetry increases [58]. However, the distance with respect to the (also more repulsive) chemical potential increases with asymmetry, providing the shift to more negative values observed in the figure.

In the case of protons, the situation for the down component is significantly different. The minimum of $\mathrm{Im}\Sigma_\downarrow$ becomes larger as the system becomes more neutron rich and the threshold is more pronounced. Consequently, the inverted peak in the real part becomes larger and more attractive. When the partial derivative is taken (right panel), similar results are obtained for all asymmetries in the energy region of interest. This indicates that the effect of asymmetry on the proton self-energy is mainly energy independent, with the real part only shifting by a constant at energies $\omega \lesssim \mu_\tau$. This is in contrast to the results for neutrons (upper right panels), where the partial derivative changes substantially as asymmetry increases, i.e., asymmetry induces energy-dependent effects for neutrons but not for protons. In spite of these qualitatively different behaviors, $n_n(0)$ and $n_p(0)$ deviate from the symmetric value by almost the same amount as asymmetry increases (see Fig. 10). Similar results have been obtained for other NN interactions under the same conditions. In the view of these results, the "universality" found for the iso-depletion for different interactions appears to be rather surprising. In spite of having very different $\mathrm{Im}\Sigma_\downarrow$ components and predicting different quasiparticle shifts, the differences in the two momentum distributions are such that they give the same results independently of the NN force.

VI. CONCLUSIONS

The aim of the present article is to provide a better understanding of the depletion of the nuclear Fermi sea as a function of density, temperature, and isospin asymmetry for different choices of realistic interactions. The SCGF method, when implemented at the level of ladder diagrams, is capable of providing answers to these questions with emphasis on the role of short-range and tensor correlations that are induced by realistic NN interactions. While long-range correlations have an additional influence on the depletion of the Fermi sea, it is expected that they are more important near the Fermi energy. For a proper comparison with finite nuclei, however, these long-range volume effects are presumably irrelevant, because they must anyway be replaced by the surface dominated physics of low-lying nuclear states. The SCGF study reported here is performed at finite temperature, on the one hand, to clarify the role of the temperature in determining depletion effects and, on the other hand, to avoid dealing with the technically challenging issue of pairing correlations. Because pairing is confined to energies very near the Fermi energy, at least at densities relevant for nuclei, our results will not be modified when such correlations will be considered in the future. We therefore report results mostly for $T = 5$ and 10 MeV, well above any pairing transition temperature for the systems under study [25]. We have studied both one-component systems (symmetric matter and pure neutron matter) as a function of density, as well as isospin-polarized matter as a function of asymmetry for normal and twice normal density.

Our results indicate that temperature affects $n(k)$ in a qualitatively similar way as dynamical correlations do. The two types of correlations, however, induce quantitatively different effects and can therefore be distinguished. To separate these components, we have relied on a comparison with the FFG results, which are only affected by temperature effects. In the degenerate regime, i.e., at high density and relatively low temperatures, temperature effects are confined to a redistribution of particles around the chemical potential within an energy scale that is proportional to the temperature considered. Dynamical correlations induced by the short-range NN repulsion and tensor effects, on the contrary, generate an almost momentum-independent depletion of the Fermi sea and, complementarily, lead to an occupation of high-momentum states far from the Fermi momentum.

The CDBonn and Av18 interactions have been employed to identify possible differences for the resulting nuclear momentum distributions. For symmetric nuclear matter and neutron matter, the depletion for $k = 0$ is strongly influenced by temperature at low densities. Once a density corresponding to $\rho = 0.08$ fm^{-3} is reached in PNM, short-range correlations lead to slowly increasing depletion as a function of density. This behavior is intuitive, because neutrons will be exposed more frequently to their mutual repulsion with increasing density, thus enhancing their occupation of high-momentum states, and, accordingly, increasing the depletion of the Fermi sea. For SNM, this behavior is *not* observed. The depletion saturates for the Av18 beyond normal density at a value of about 12%, while it continues to *decrease* for CDBonn. The larger depletion of the Av18 as compared to CDBonn further emphasizes that the first is a slightly harder NN interaction. This is also illustrated by the different behavior of their self-energies. To understand this puzzling density dependence, we have utilized an approximate relation between the momentum distribution and energy derivatives of the real part of the time-ordered self-energy taken at the corresponding quasiparticle energy (emphasizing the importance of self-consistency). For momenta below k_F, this result is valid when the energy dependence of the real part of the self-energy associated (through a dispersion integral) with the imaginary part above the chemical potential is essentially linear. For momenta above k_F, a similar relation holds when the real part of the self-energy is considered that is related to the imaginary part below the chemical potential. Near the Fermi momentum and at low densities, this approximation ceases to be valid. However, for most situations considered in this article, it provides an excellent approximation to the momentum distribution calculated from the self-consistent spectral function.

To utilize this relation, we have generated the time-ordered contributions to the nucleon self-energy at finite temperature. This allows us to gain access to the appropriate energy derivatives. Finite-temperature calculations are normally performed with retarded quantities, but the "particle" and "hole" decomposition of the self-energy provides a more suitable connection with the corresponding results at zero temperature. The relevant self-energy components for determining the occupation inside the Fermi sea indeed shed light on the anomalous density dependence of the depletion in symmetric nuclear matter. Mainly due to the tensor force, there is a an important threshold behavior in the imaginary part of the self-energy above the chemical potential in symmetric matter, which is absent in neutron matter. For CDBonn, the threshold gives rise to an inverted peak in the corresponding real part that moves to higher energy with increasing density, yielding an almost density independent derivative. Because the tensor force also leads to more binding with increasing density, the location of the derivative moves farther away from the peak with density, thereby decreasing its absolute value and accordingly the depletion of the Fermi sea. For the Av18 interaction, the energy derivative decreases with density on account of its less dramatic threshold behavior for the imaginary part, yielding similar binding from an imaginary part that is significantly stronger than for CDBonn, but peaking at much higher energy. Because the binding effects are similar to those for CDBonn, the two effects compensate leading to the saturating behavior of the depletion observed in Fig. 2. For neutron matter, the $^3S_1$-$^3D_1$ coupled partial wave is absent and no strong threshold behavior is generated in the imaginary part for both interactions. This leads to the more intuitive behavior that the depletion increases with the density.

For asymmetric systems, we find a significant change of depletion with isospin asymmetry. We identify a temperature effect for the minority protons (but not for the majority neutrons) at an asymmetry beyond $\alpha = 0.4$ at $T = 5$ MeV and normal density, due to the corresponding low density for protons. For twice normal density, the temperature effect does not play a role up to an extreme asymmetry of 0.8. The effect was implicit (and stronger) in earlier results obtained at $T = 10$ MeV [24]. The remaining difference between the neutron and proton depletion is due to the decreased (increased) importance of tensor correlations for neutrons (protons). By considering also different operatorial clones of the Av18 interaction, like Av8′, Av6′, and Av4′, we can indeed unambiguously demonstrate that this difference is associated with the tensor force. More importantly, this iso-depletion is independent of the chosen interaction and therefore determined solely by phase shifts at least up to twice normal density.

We close this discussion by noting that the employed interactions appear to slightly underestimate the depletion of the experimentally determined depletion of the deep proton mean-field orbits in ^{208}Pb [16]. Interactions with an even stronger repulsion, like the Reid soft core [73], yield a slightly larger depletion of about 15% [27,34,74]. Nevertheless, while there remains a few percentages of uncertainty as to the exact amount that is experimentally required, it is also clear that very different interactions, including modern ones, still lead to very similar predictions for the depletion of the nuclear Fermi sea. Such depletions can be reliably calculated with the SCGF method. When lattice QCD calculations yield unambiguous information about the short-range NN repulsion, the remaining uncertainty about the depletion of the nuclear Fermi sea might eventually be eliminated.

ACKNOWLEDGMENTS

This work was partially supported by the US National Science Foundation under Grant Nos. PHY-0555893, PHY-0800026, and PHY-0652900 and by MICINN (Spain) under projects FIS2008-01661 and CPAN CSD2007-00042 Programa Consolider-Ingenio 2010.

[1] D. Rohe *et al.*, Phys. Rev. Lett. **93**, 182501 (2004).
[2] H. Müther, A. Polls, and W. H. Dickhoff, Phys. Rev. C **51**, 3040 (1995).
[3] I. Sick, S. Fantoni, A. Fabrocini, and O. Benhar, Phys. Lett. **B323**, 267 (1994).
[4] C. J. G. Onderwater *et al.*, Phys. Rev. Lett. **81**, 2213 (1998).
[5] R. Starink *et al.*, Phys. Lett. **B474**, 33 (2000).
[6] C. Giusti, F. D. Pacati, K. Allaart, W. J. W. Geurts, W. H. Dickhoff, and H. Müther, Phys. Rev. C **57**, 1691 (1998).
[7] C. Barbieri, C. Giusti, F. D. Pacati, and W. H. Dickhoff, Phys. Rev. C **70**, 014606 (2004).
[8] R. Subedi *et al.*, Science **320**, 1476 (2008).
[9] R. Schiavilla, R. B. Wiringa, S. C. Pieper, and J. Carlson, Phys. Rev. Lett. **98**, 132501 (2007).
[10] L. Frankfurt, M. Sargsian, and M. Strikman, Int. J. Mod. Phys. A **23**, 2991 (2008).
[11] B. E. Vonderfecht, W. H. Dickhoff, A. Polls, and A. Ramos, Phys. Rev. C **44**, R1265 (1991).
[12] S. Fantoni and V. R. Pandharipande, Nucl. Phys. **A427**, 473 (1984).
[13] P. Grangé, J. Cugnon, and A. Lejeune, Nucl. Phys. **A473**, 365 (1987).
[14] O. Benhar, A. Fabrocini, and S. Fantoni, Phys. Rev. C **41**, R24 (1990).
[15] M. Baldo, I. Bombaci, G. Giansiracusa, U. Lombardo, C. Mahaux, and R. Sartor, Phys. Rev. C **41**, 1748 (1990).
[16] M. F. van Batenburg, Ph.D. thesis, University of Utrecht (2001).
[17] L. Lapikás *et al.*, Phys. Rev. Lett. (will be submitted during 2009).
[18] F. Mazzanti, A. Polls, J. Boronat, and J. Casulleras, Phys. Rev. Lett. **92**, 085301 (2004).
[19] C. Barbieri, D. Van Neck, and W. H. Dickhoff, Phys. Rev. A **76**, 052503 (2007).
[20] N. Ishii, S. Aoki, and T. Hatsuda, Phys. Rev. Lett. **99**, 022001 (2007).
[21] R. Machleidt, F. Sammarruca, and Y. Song, Phys. Rev. C **53**, R1483 (1996).
[22] R. Machleidt, Phys. Rev. C **63**, 024001 (2001).
[23] D. R. Entem and R. Machleidt, Phys. Rev. C **68**, 041001(R) (2003).

[24] T. Frick, H. Müther, A. Rios, A. Polls, and A. Ramos, Phys. Rev. C **71**, 014313 (2005).
[25] H. Müther and W. H. Dickhoff, Phys. Rev. C **72**, 054313 (2005).
[26] R. B. Wiringa, V. G. J. Stoks, and R. Schiavilla, Phys. Rev. C **51**, 38 (1995).
[27] W. H. Dickhoff and C. Barbieri, Prog. Part. Nucl. Phys. **52**, 377 (2004).
[28] E. R. Stoddard, Ph.D. thesis, Washington University in St. Louis (2000).
[29] T. Frick and H. Müther, Phys. Rev. C **68**, 034310 (2003).
[30] T. Frick, Ph.D. thesis, University of Tübingen (2004).
[31] A. Rios, Ph.D. thesis, University of Barcelona (2007).
[32] L. P. Kadanoff and G. Baym, *Quantum Statistical Mechanics* (Benjamin, New York, 1962).
[33] G. Baym, Phys. Rev. **127**, 1391 (1962).
[34] Y. Dewulf, W. H. Dickhoff, D. Van Neck, E. R. Stoddard, and M. Waroquier, Phys. Rev. Lett. **90**, 152501 (2003).
[35] A. Gade *et al.*, Phys. Rev. Lett. **93**, 042501 (2004).
[36] R. J. Charity, L. G. Sobotka, and W. H. Dickhoff, Phys. Rev. Lett. **97**, 162503 (2006).
[37] R. J. Charity, J. M. Mueller, L. G. Sobotka, and W. H. Dickhoff, Phys. Rev. C **76**, 044314 (2007).
[38] J. Haidenbauer and W. Plessas, Phys. Rev. C **30**, 1822 (1984).
[39] M. Lacombe, B. Loiseau, J. M. Richard, R. Vinh Mau, J. Côté, P. Pirés, and R. de Tourreil, Phys. Rev. C **21**, 861 (1980).
[40] A. L. Fetter and J. D. Walecka, *Quantum Theory of Many-Particle Systems* (Dover, New York, 2003).
[41] W. H. Dickhoff and D. Van Neck, *Many-Body Theory Exposed!* (World Scientific, Singapore, 2008), 2nd ed.
[42] G. D. Mahan, *Many-Particle Physics* (Plenum Press, New York, 1981).
[43] G. Baym and N. D. Mermin, J. Math. Phys. **2**, 232 (1961).
[44] A. Schnell, T. Alm, and G. Röpke, Phys. Lett. **B387**, 443 (1996).
[45] P. Bożek, Phys. Rev. C **59**, 2619 (1999).
[46] A. Ramos, A. Polls, and W. H. Dickhoff, Nucl. Phys. **A503**, 1 (1989).
[47] Y. Dewulf, D. Van Neck, and M. Waroquier, Phys. Rev. C **65**, 054316 (2002).
[48] A. Polls, A. Ramos, J. Ventura, S. Amari, and W. H. Dickhoff, Phys. Rev. C **49**, 3050 (1994).
[49] T. Frick, H. Müther, and A. Polls, Phys. Rev. C **69**, 054305 (2004).
[50] P. Bożek and P. Czerski, Eur. Phys. J. A **11**, 271 (2001).
[51] A. Rios, A. Polls, A. Ramos, and H. Müther, Phys. Rev. C **74**, 054317 (2006).
[52] D. J. Thouless, Ann. Phys. **10**, 553 (1960).
[53] T. Alm, G. Röpke, A. Schnell, N. H. Kwong, and H. S. Köhler, Phys. Rev. C **53**, 2181 (1996).
[54] V. M. Galitskii and A. B. Migdal, J. Exp. Theor. Phys. **7**, 96 (1958).
[55] D. S. Koltun, Phys. Rev. C **9**, 484 (1974).
[56] J. M. Luttinger and J. C. Ward, Phys. Rev. **118**, 1417 (1960).
[57] P. Bożek, Phys. Lett. **B586**, 239 (2004).
[58] A. Rios, A. Polls, and H. Müther, Phys. Rev. C **73**, 024305 (2006).
[59] A. Mukherjee and V. R. Pandharipande, Phys. Rev. C **75**, 035802 (2007).
[60] A. Lejeune, P. Grangé, M. Martzolff, and J. Cugnon, Nucl. Phys. **A453**, 189 (1986).
[61] H. Müther and A. Polls, Prog. Part. Nucl. Phys. **45**, 243 (2000).
[62] R. B. Wiringa and S. C. Pieper, Phys. Rev. Lett. **89**, 182501 (2002).
[63] V. G. J. Stoks, R. A. M. Klomp, C. P. F. Terheggen, and J. J. de Swart, Phys. Rev. C **49**, 2950 (1994).
[64] A. Rios, A. Polls, and I. Vidaña, Phys. Rev. C **79**, 025802 (2009).
[65] C. Horowitz and A. Schwenk, Phys. Lett. **B638**, 153 (2006).
[66] A. Ramos, W. H. Dickhoff, and A. Polls, Phys. Rev. C **43**, 2239 (1991).
[67] R. Sartor and C. Mahaux, Phys. Rev. C **21**, 1546 (1980).
[68] J. Hüfner and C. Mahaux, Ann. Phys. **73**, 525 (1972).
[69] M. Baldo, I. Bombaci, G. Giansiracusa, and U. Lombardo, Nucl. Phys. **A530**, 135 (1991).
[70] M. Baldo, I. Bombaci, G. Giansiracusa, U. Lombardo, C. Mahaux, and R. Sartor, Nucl. Phys. **A545**, 741 (1992).
[71] C. Mahaux and R. Sartor, Phys. Rep. **211**, 53 (1992).
[72] B. E. Vonderfecht, W. H. Dickhoff, A. Polls, and A. Ramos, Nucl. Phys. **A555**, 1 (1993).
[73] R. V. Reid, Ann. Phys. **50**, 411 (1968).
[74] W. H. Dickhoff and E. P. Roth, Acta Phys. Pol. B **33**, 65 (2002).